Full paper

Tunnel structured manganese oxide nanowires as redox active electrodes for hybrid capacitive deionization

Bryan W. Byles[a], David A. Cullen[b], Karren L. More[c], Ekaterina Pomerantseva[a],*

[a] Department of Materials Science and Engineering, Drexel University, Philadelphia, PA 19104, USA
[b] Materials Science and Technology Division, Oak Ridge National Laboratory, Oak Ridge, TN 37831, USA
[c] Center for Nanophase Materials Sciences, Oak Ridge National Laboratory, Oak Ridge, TN 37831, USA

ARTICLE INFO

ABSTRACT

Hybrid capacitive deionization (HCDI), which combines a capacitive carbon electrode and a redox active electrode in a single device, has emerged as a promising method for water desalination, enabling higher ion removal capacity than devices containing two carbon electrodes. However, to date, the desalination performance of few redox active materials has been reported. For the first time, we present the electrochemical behavior of manganese oxide nanowires with four different tunnel crystal structures as faradaic electrodes in HCDI cells. Two of these phases are square tunnel structured manganese oxides, α-MnO$_2$ and todorokite-MnO$_2$. The other two phases have novel structures that cross-sectional scanning transmission electron microscopy analysis revealed to have ordered and disordered combinations of structural tunnels with different dimensions. The ion removal performance of the nanowires was evaluated not only in NaCl solution, which is traditionally used in laboratory experiments, but also in KCl and MgCl$_2$ solutions, providing better understanding of the behavior of these materials for desalination of brackish water that contains multiple cation species. High ion removal capacities (as large as 27.8 mg g^{-1}, 44.4 mg g^{-1}, and 43.1 mg g^{-1} in NaCl, KCl, and MgCl$_2$ solutions, respectively) and high ion removal rates (as large as 0.112 mg g^{-1} s^{-1}, 0.165 mg g^{-1} s^{-1}, and 0.164 mg g^{-1} s^{-1} in NaCl, KCl, and MgCl$_2$ solutions, respectively) were achieved. By comparing ion removal capacity to structural tunnel size, it was found that smaller tunnels do not favor the removal of cations with larger hydrated radii, and more efficient removal of larger hydrated cations can be achieved by utilizing manganese oxides with larger structural tunnels. Extended HCDI cycling and ex situ X-ray diffraction analysis revealed the excellent stability of the manganese oxide electrodes in repeated ion removal/ion release cycles, and compositional analysis of the electrodes indicated that ion removal is achieved through both surface redox reactions and intercalation of ions into the structural tunnels. This work contributes to the understanding of the behavior of faradaic materials in electrochemical water desalination and elucidates the relationship between the electrode material crystal structure and the ion removal capacity/ion removal rate in various salt solutions.

1. Introduction

The scarce availability of freshwater has become a critical issue for society as population levels increase, water consumption levels scale up with living standards, and pollution destroys many natural sources. Nearly four billion people face water scarcity at least one month out of the year and half a billion people face water scarcity year round [1], and the World Economic Forum has repeatedly identified a water crisis as one of the largest global risks in regards to its potential impact [2]. Thus, the development of desalination techniques that can efficiently provide freshwater at significant scales from salt water (which constitutes 97% of the water available on Earth [3]) are imperative for

achieving an adequate supply of water for the world's population.

Commonly utilized large-scale desalination techniques involve reverse osmosis and thermal separation methods. These techniques, which remove the water (majority phase) from the salt (minority phase), have downsides including high energy consumption and complex operation [4–7]. At lower salt concentrations, such as those found in brackish water, it becomes energetically favorable to remove the salt from the water. An emerging and attractive process for salt removal is capacitive deionization (CDI). CDI is a low pressure and room temperature process in which water is flown between or through electrodes while a potential is applied. When a positive potential is applied, ions are removed from the water via electric double layer adsorption or

chemical reaction with the electrode material. When the potential is released or reversed, ions are forced off of the electrodes, thus re-generating them for subsequent cycling. Advantages of CDI include no secondary pollution, lower energy consumption when compared to current desalination techniques, and the potential for energy recovery from charge stored in the electrodes during ion removal [4–6]. Thus, CDI is of significant interest for development as a large-scale desalination technique.

CDI typically involves the use of high surface area carbon materials as electrodes [4–6]. These materials remove ions via adsorption in the electric double layer on the surface of the electrodes, and ion removal capacities as high as 21.0 mg of salt (NaCl) per gram of electrode have been reported for a nitrogen doped graphene sponge [8]. Further, through incorporation of ion exchange membranes in a configuration termed membrane capacitive deionization (MCDI), the efficiency of CDI systems based on carbon materials can be improved [5,6]. However, similar to supercapacitors, carbon based materials are limited in their salt adsorption capacity by the surface area available for ion absorption [6,9]. This limitation can be overcome by utilizing electrode materials that undergo faradaic reactions with ions in solution. Such chemical reactions can occur throughout the bulk of the structure and thus are not limited by surface area. Another approach to desalination, termed desalination batteries, uses a similar configuration as traditional CDI, but instead of high surface area capacitive electrodes, two faradaic materials are utilized as electrodes. Desalination batteries have shown higher ion removal capacities but slower ion removal rates due to the sluggish kinetics of ion intercalation compared to adsorption onto a material's surface [10–13]. More recently, an approach termed hybrid capacitive deionization (HCDI) has emerged [9], which combines one faradaic electrode and one carbon electrode (Fig. 1). HCDI systems have shown improved ion removal capacities over conventional CDI systems that solely use carbon electrodes, as well as higher ion removal rates compared to desalination batteries, thus combining the best attributes of both desalination approaches [9,14].

One promising class of materials for removal of ions from aqueous solution is manganese oxides, demonstrated by past research directed at this material system for water desalination [9–11,13]. Several advantages are associated with utilizing manganese oxides as electrodes for HCDI systems. First, manganese oxides are a structurally diverse class of materials, with over 30 known polymorphs [15], resulting in a wide range of crystal structures and chemistries that can be investigated and tailored for ion removal in an HCDI system. Second, the inherent low cost and low toxicity of manganese oxides are advantageous

properties when considering large-scale commercial application of HCDI systems. Third, the high electrochemical activity of manganese oxides enabled by the Mn^{3+}/Mn^{4+} redox pair presents the potential for high ion removal capacity [16,17]. Fourth, the stability of manganese oxides in aqueous environments [18] allows for their extended application under potential for ion removal from aqueous solutions, and the hydrophilic nature of manganese oxide surfaces results in manganese oxide particles being easily wetted with solution to maximize utilization of active material [19,20]. Such a combination of properties thus makes manganese oxides exceptionally attractive materials for water desalination applications.

Within manganese oxides there is a unique family of materials with tailorable tunnel crystal structures, tunnel structured manganese oxides (TuMOs). These phases, several of which are shown schematically in Fig. S1, are built from MnO_6 octahedra sharing corners and edges to form structural tunnels with different sizes and shapes. The large tunnels contain positively charged cations that stabilize the crystal structure of the material and thus are often called "stabilizing ions". Past work has demonstrated that these open tunnel structures show excellent cation exchange properties [21,22] and have been utilized effectively as battery [17,23–25] and supercapacitor [17,18,26] electrodes. Therefore, it is believed that TuMOs can show high performance in water desalination applications, with the large, open tunnel structures providing ample crystallographic volume to store ions removed from solution. Moreover, variation of the synthesis conditions and stabilizing ions provides control over the specific size, shape, and ionic content of the structural tunnels, presenting a degree of tunability that makes TuMOs an ideal materials system for exploring the relationship between crystal structure and ion removal capacity/selectivity. Another unique advantage of TuMOs is that they can all be synthesized with a flexible nanowire morphology that allows for excellent access of solution and ions to material's surfaces. Notably, $Na_{0.44}MnO_2$ powder, which exhibited an ion removal capacity of 31.2 mg g^{-1} in NaCl [9], is a member of this materials family, indicating the potential of TuMOs for water desalination applications and providing further reason to investigate the behavior of materials with different tunnel crystal structures. However, except for $Na_{0.44}MnO_2$, no other TuMO phases have been evaluated for HCDI application.

In this report, we present for the first time the performance of TuMOs that contain tunnels of different dimensions, including α-MnO_2 and manganese oxide with todorokite crystal structure. Further, two novel hybrid tunnel structures with ordered and disordered combinations of 2×n and 3×n tunnels (n = 2, 3, 4, 5, 6) within individual
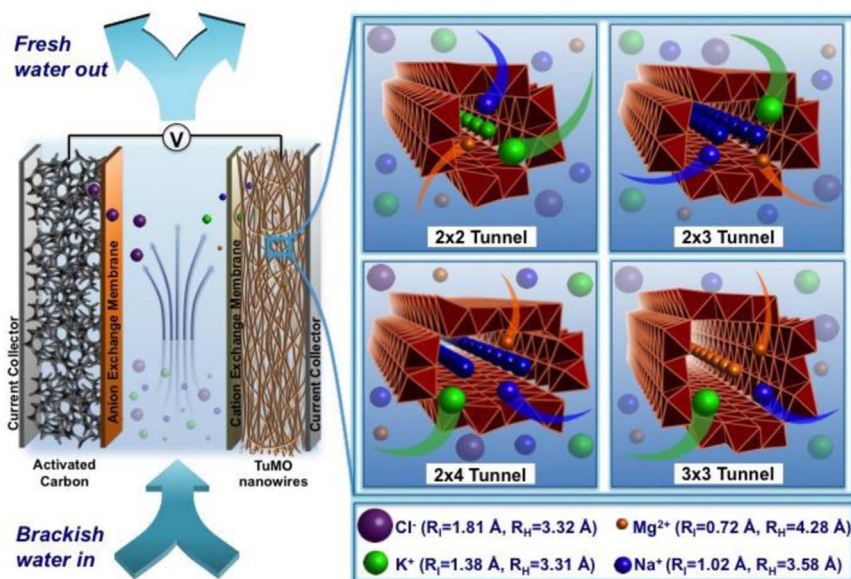

Fig. 1. Schematic illustration of ion removal from water via a hybrid capacitive deionization (HCDI) cell. As brackish water is flown into the cell, an electric potential is applied across the two electrodes. In the carbon electrode, ions are adsorbed on the surface of the activated carbon. In the manganese oxide nanowire electrode, ions chemically react with the surface or intercalate into the structure of the TuMO nanowires, as is shown on the right. The tunnel size is defined by the number of MnO_6 octahedra on perpendicular sides of the rectangular tunnels ("X" octahedra × "Y" octahedra). The ionic radius (R_I) [29] and hydrated radius (R_H) [30] are shown for Cl$^-$, K$^+$, Mg^{2+}, and Na$^+$ ions. A coordination of VI is assumed for ionic radii.

nanowires are synthesized and investigated for the first time. Utilizing an HCDI configuration, illustrated in Fig. 1, the ion removal performance of these materials is studied in aqueous solutions of NaCl, KCl, and MgCl$_2$, which were chosen due to the common presence of Na$^+$, K$^+$, Mg^{2+}, and Cl$^-$ ions in saline and polluted waters [27,28]. High ion removal capacities and ion removal rates are achieved for each material, demonstrating the advantage of utilizing such redox active electrodes in HCDI for different ionic solutions. Combined structural, chemical, and electrochemical analysis of the electrodes provides insight into the stability and mechanism of ion removal exhibited by the TuMOs.

2. Materials and methods

2.1. Materials synthesis

α-MnO$_2$ nanowires were prepared by a hydrothermal synthesis method described elsewhere [31] in which 316 mg of KMnO$_4$ (Acros Organics) and 108 mg of NH$_4$Cl (Strem Chemicals) were dissolved in 100 mL of deionized water. 20 mL of this solution was added into 23 mL Teflon-lined stainless steel autoclaves (Parr Instruments) that were heated at 150 °C for 48 h. The product was then filtered, washed, and dried at 100 °C for 12 h.

Manganese oxide nanowires with todorokite crystal structure (Tod-MnO$_2$) were synthesized via a process described in a previous work [23]. The precursor material, Na-birnessite, was prepared via a method described elsewhere [32] in which a mixed solution of 0.6 M NaOH (Acros Organics) and 2 M H$_2$O$_2$ (Fisher Scientific) having a volume of 100 mL was added dropwise to a solution of 0.3 M Mn(NO$_3$)$_2$ (Acros Organics). After washing and filtering, the Na-birnessite was then placed in 1 L of 1 M MgCl$_2$ (Sigma Aldrich) solution to perform an ion exchange reaction. After 24 h of stirring in solution, the products were filtered out and placed in a fresh 1 L solution of 1 M MgCl$_2$ for an additional 24 h, resulting in a total ion exchange time of 48 h and conversion of the Na-birnessite into Mg-buserite. 50 mg of the Mg-buserite was added to 17 mL of 1 M MgCl$_2$ in a 23 mL Teflon-lined stainless steel autoclave followed by hydrothermal treatment at 220 °C for 96 h. The resulting product was then filtered, washed, and dried at 100 °C for 12 h.

The two other TuMO phases investigated in this work were synthesized via hydrothermal treatment of Na-birnessite precursor, based on a previously reported process [33]. The Na-birnessite was made following the same procedures as for the Tod-MnO$_2$ nanowires. When the precipitate was allowed to statically age for only one hour before filtering and thorough washing, low crystallinity birnessite (LC-Bir) was created. The LC-Bir was then allowed to dry at 100 °C for 12 h before 100 mg of this powder was mixed into 15 mL of deionized water, added to a 23 mL Teflon-lined stainless steel autoclave, and hydrothermally treated at 220 °C for 8 days. After hydrothermal treatment, the product was filtered, washed, and dried at 100 °C for 12 h. The resulting material was termed "Hybrid-MnO$_2$" nanowires, and the structure of this material is described in detail in Section 3. Increasing the length of the aging step in the birnessite synthesis from 1 h to 96 h resulted in the formation of a Na-birnessite with higher crystallinity (HC-Bir). When the HC-Bir was hydrothermally treated under the same conditions as the LC-Bir, TuMO nanowires with a greater degree of structural regularity, termed "2×n-MnO$_2$" nanowires were formed. The structure of this phase is also discussed in Section 3.

2.2. Materials characterization

X-ray powder diffraction (XRD) for phase analysis was performed using a Rigaku SmartLab X-ray diffractometer (Japan) with copper Kα radiation, a step size of 0.02°, and step time of 1 s. The morphology of all samples was characterized via scanning electron microscopy (SEM) using a Zeiss Supra 50VP (Germany) equipped with an energy dispersive X-ray (EDX) spectrometer. EDX spectroscopy allowed for the evaluation of the chemical composition of the electrode materials before and after ion removal experiments. For analysis of the cycled manganese oxide electrodes, the electrodes were thoroughly washed with deionized water to remove physisorbed ions. For each sample, EDX spectra were recorded in multiple 10 μm by 10 μm regions, and the chemical composition was determined by averaging the quantification of all spectra for a given sample. Cross-sections of the four manganese oxide nanowire phases were prepared for aberration-corrected scanning transmission electron microscopy (STEM) by diamond-knife ultramicrotomy. High-angle annular dark-field (HAADF) images were acquired using a JEOL JEM 2200FS TEM/STEM operated at 200 kV and equipped with a CEOS probe Cs-corrector.

2.3. Electrode preparation

Electrodes of all materials (α-MnO$_2$, Tod-MnO$_2$, 2×n-MnO$_2$, Hybrid-MnO$_2$, and activated carbon (YP-50F, Kuraray Chemical)) were prepared using the same method. The active material, carbon black (Alfa Aesar), and polytetrafluoroethylene binder (Sigma Aldrich, 60 wt % in H$_2$O) were thoroughly mixed in a 80:15:5 ratio, respectively, in ethanol to form a paste, which was then rolled out to form 150–300 μm thick electrode films. After drying the films at 100 °C for 24 h, individual electrodes were cut with an area of approximately 340 mm^2 for the manganese oxides (approximate mass of ~50 mg) and 650 mm^2 for the activated carbon (approximate mass of ~100 mg). Different size films were cut for the negative and positive electrodes because of the cell geometry and to ensure a larger mass of the activated carbon electrode, which is the limiting factor in the capacity of the HCDI system due to the surface-based ion removal mechanism characteristic of carbon materials [9,14].

2.4. Ion removal experiments

The custom-designed cell for HCDI tests is shown schematically in Fig. 2. Ion removal experiments were performed in batch mode configuration with a 15 mL ionic solution reservoir. Solutions of 15 mM
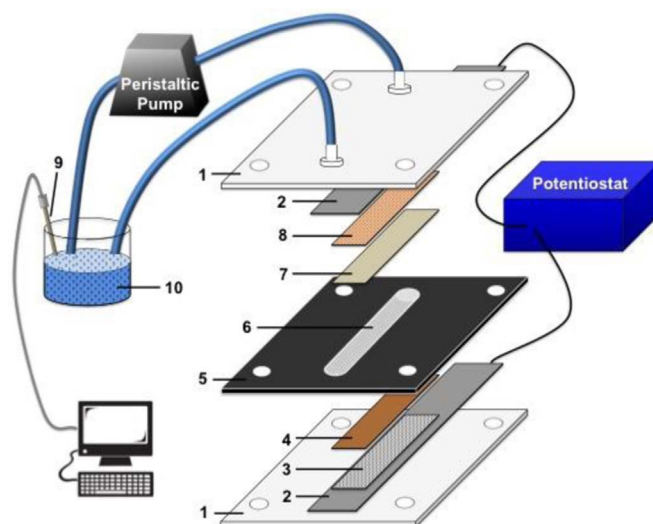

Fig. 2. Schematic illustration of the HCDI cell used for evaluating the ion removal behavior of all TuMO nanowires investigated in this work. The deionization cell consisted of Delrin exterior (McMasterCarr, USA) (1), conductive tin plated tape as the current collector (3 M™) (2), activated carbon electrode (3), anion exchange membrane (AMV, Selemion, AGC engineering Co.) (4), Viton fluoroelastomer gasket (500 μm thickness, McMasterCarr, USA) with a precut flow channel (area of flow channel = 294 mm^2) (5), nylon spacers (Spectrum Laboratories, Inc., USA) (6), cation exchange membrane (CMV, Selemion, AGC engineering Co.) (7), manganese oxide electrode (8), dip-in conductivity probe (ET915, eDAQ Pty Ltd, Australia) (9), and salt solution reservoir (10).

NaCl, KCl, or MgCl$_2$ (Fisher Scientific and Acros Organics) were pumped through the cell using a peristaltic pump at 20 mL min^{-1} flow rate to probe the ion removal performance of the manganese oxides in different salt solutions. Experiments were performed in a constant voltage operation mode, alternating between 15 min ion removal step at 1.2 V and 15 min ion release step at − 1.2 V. Applied potentials of 1.2 V and − 1.2 V were chosen to maximize ion removal capacity while remaining within the electrolysis stability window of water [5,6]. A VMP3 potentiostat/galvanostat (BioLogic, France) was used to apply potential and monitor current in the cell. The conductivity of the salt solution reservoir was monitored using a dip-in conductivity probe (Fig. 2). While both the initial conductivity and concentration of the salt solution can affect the performance of the desalination device, in this study, the initial concentration of the solutions containing different cations was fixed. This was done to control for the different molar masses of the salts and allow for comparison of the desalination performance of a given material across solutions containing various ionic species.

The conductivity of the salt solutions was converted to the concentration of salt present in the solutions via conductivity/concentration relationships determined using a Malvern Instruments Zetasizer Nano ZS equipped with a MPT-2 Multi Purpose Titrator. This titration method produced concentrations vs. conductivity plots in the concentration range of 1–1600 mg L^{-1} for NaCl and KCl and 1–3000 mg L^{-1} for MgCl$_2$ (Fig. S2). From these plots, the linear relationship between concentration and conductivity can be extracted. This relationship is applied to conductivity data recorded during ion removal experiments to obtain concentration vs. time profiles, from which performance parameters were calculated.

The ion removal capacity (in mg of salt per g of electrode material) of the HCDI system was calculated using Eq. (1) [9], where C_0 and C_i are the salt concentrations at the beginning and end of an ion removal step, respectively, V is the volume of the solution being tested, and M_{tot} is the total mass of the manganese oxide and activated carbon electrodes in the flow channel of the cell (~ 70 to 80 mg), including the binder and carbon additives.

$$\textbf{Ion removal } \text{capacity} \left(\frac{\text{mg}}{\text{g}}\right) = \frac{(C_0 - C_i)*V}{M_{tot}} \quad (1)$$

The ion removal rate was calculated by dividing the ion removal capacity by the step time (s) [9], and the maximum ion removal rate can be extracted as the maximum of the ion removal rate vs. step time curve.

Charge efficiency (Λ) of the HCDI system was calculated from the ratio of the amount of salt removed to the charge passed through the cell during a given ion removal step [5,6]. Eq. (2) is derived from this ratio and can be used to calculate Λ, where C_0 and C_i are the salt concentrations at the beginning and end of an ion removal step, respectively, V is the volume of the solution being tested, F is Faraday's constant, M_S is the molar mass of the salt in solution, and Σ is the charged passed during the ion removal step (obtained from integrating the current passed during the ion removal step with respect to time).

$$\Lambda = \frac{(C_0 - C_i)*V*F}{M_S*\Sigma} \quad (2)$$

At the beginning of each test, several ion removal/ion release cycles were performed until a "dynamic steady state" condition [34] was reached in which the net change in conductivity during the ion removal and ion release steps was nearly equivalent. All reported ion removal performance was obtained under these conditions, and all experiments were triplicated in order to ensure reproducibility.
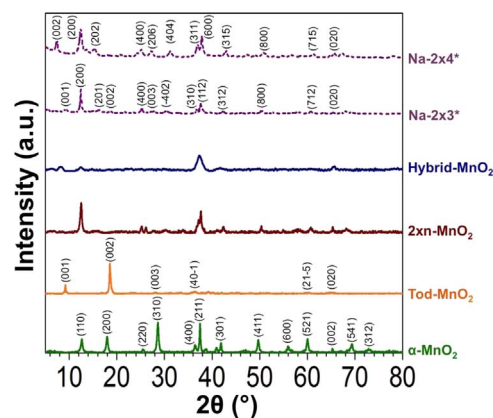

Fig. 3. XRD patterns of α-MnO$_2$, Tod-MnO$_2$, 2×n-MnO$_2$, and Hybrid-MnO$_2$ phases. *XRD patterns of Na-2×3 and Na-2×4 are taken from a previous report [33] and are shown for comparison.

3. Results

3.1. Material characterization

Fig. 3 shows the XRD patterns of the TuMO phases synthesized in this work. The XRD patterns of α-MnO$_2$ and manganese oxide with todorokite crystal structure (Tod-MnO$_2$) show strong reflections that correspond well to past reports for the two respective materials [21,24,31,35–37]. The XRD patterns of α-MnO$_2$ and Tod-MnO$_2$ can be readily indexed to a tetragonal $I4/m$ phase (JCPDS file #44-014) and a monoclinic $P2/m$ phase (JCPDS file #38-475), respectively. Initial efforts, with a LC-Bir precursor, to synthesize a previously reported Na-2×3 phase with 2×3 structural tunnels [33] resulted in a material (Hybrid-MnO$_2$) with an XRD pattern exhibiting only a few, broad reflections, indicating poor long-range order within the material structure. In an effort to improve the crystallinity of this material and obtain the targeted Na-2×3 phase, the HC-Bir precursor was used during synthesis, resulting in a material (2×n-MnO$_2$) with an XRD pattern showing a greater number of peaks with decreased widths compared to the XRD pattern for the Hybrid-MnO$_2$ phase (Fig. 3). Although the crystallinity of the 2×n-MnO$_2$ phase was improved, the XRD pattern of this material still did not match the previously reported pattern for Na-2×3 (Fig. 3). The XRD patterns of 2×n-MnO$_2$ and Na-2×3 do share many common reflections, but the reflection at ~ 9.2° 2θ (~ 9.6 Å), corresponding to a spacing of three MnO$_6$ octahedra ((001) reflection), was not found in the 2×n-MnO$_2$ phase. The 9.6 Å spacing is a defining structural reflection for the 3 octahedra side length of the characteristic 2×3 tunnels in the Na-2×3 phase.

SEM images (Fig. 4a–d) revealed that the morphology of all four manganese oxide phases, including the 2×n-MnO$_2$ and Hybrid-MnO$_2$ phases, is that of well-formed nanowires with sharply defined edges, indicating crystalline materials. The important discrepancy between XRD patterns of the 2×n-MnO$_2$ phase and Na-2×3 in past reports, as well as the discrepancy between the poorly crystalline XRD pattern for the Hybrid-MnO$_2$ phase and its well-defined nanowire morphology, prompted utilization of cross-sectional STEM analysis to further evaluate the structure of the synthesized materials.

Cross-sectional HAADF-STEM images of the nanowires are shown in Fig. 4e–h. In these images, the longitudinal axis of the nanowires is oriented parallel to the electron beam, revealing the atomic arrangement in the cross-section of the nanowire and allowing for evaluation of the differences in the size, shape, and distribution of the structural tunnels in each material. Fig. 4e shows a cross-sectional STEM image of α-MnO$_2$, where 2×2 tunnels typical for α-MnO$_2$ can be clearly observed. The 8 Mn columns (denoted by green circles) are arranged in a square 2×2 fashion with a tunnel side length of 4.6 Å (structural schematic in Fig. S1a). This tunnel structure is consistent throughout
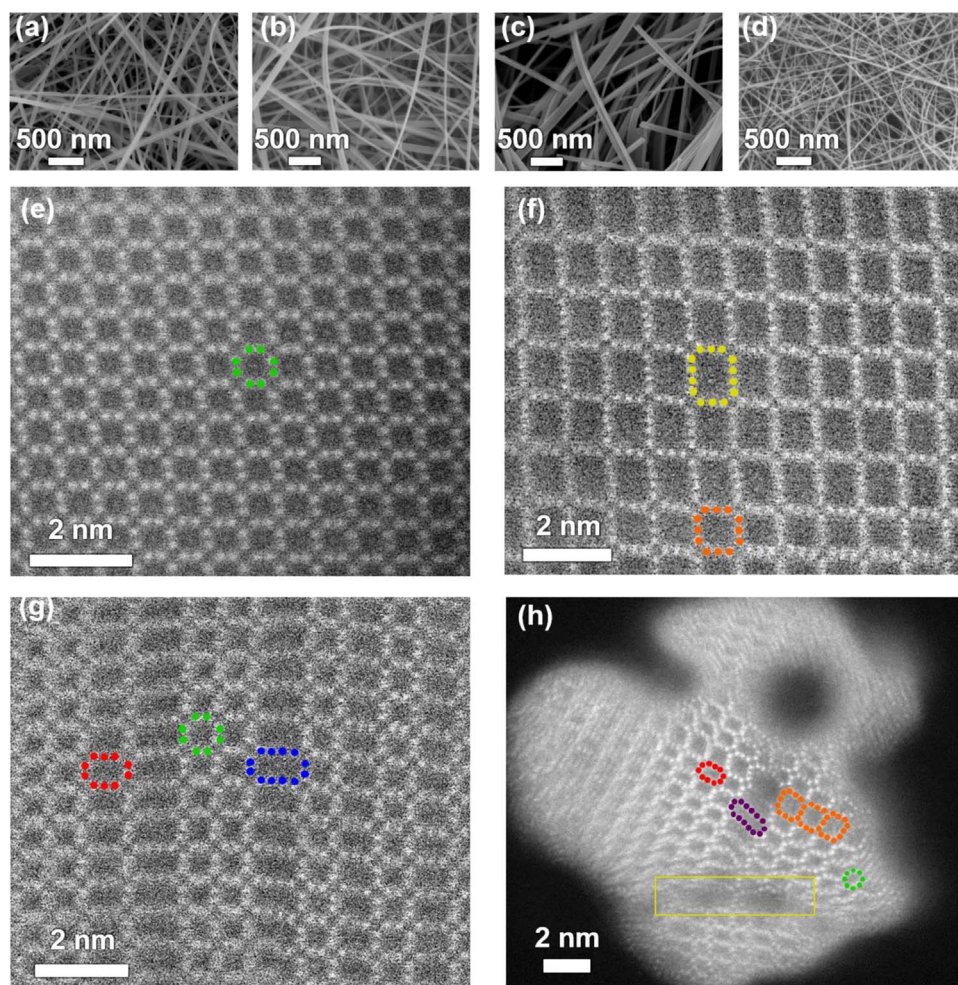
Fig. 4. SEM (a–d) and cross-sectional HAADF-STEM (e-h) images of α-MnO$_2$, Tod-MnO$_2$, 2×n-MnO$_2$, and Hybrid-MnO$_2$: (a, e) α-MnO$_2$, (b, f) Tod-MnO$_2$, (c, g) 2×n-MnO$_2$, and (d, h) Hybrid MnO$_2$. Colored circles corresponding to Mn columns denote structural tunnels with different dimensions: green − 2×2 tunnels, red − 2×3 tunnels, blue − 2×4 tunnels, purple − 2×5 tunnels, orange − 3×3 tunnels, and yellow − 3×4 tunnels. The yellow box in (h) shows an area within the nanowire with incompletely formed tunnels.

the entire nanowire (additional STEM images in Fig. S3a), confirming that this material is composed of 2×2 tunnels, which is in agreement with XRD data in Fig. 3.

Fig. 4f shows a cross-sectional STEM image of Tod-MnO$_2$. Although manganese oxide with todorokite crystal structure is believed to be built by 3×3 tunnels [21,37], previous reports have shown that the 3×3 tunnels can coexist with tunnels of multiple different 3×n (n = 3, 4, 5, 6, 7) dimensions due to incomplete transformation from the layered Mg-buserite precursor [24,35,36]. We also find the presence of several 3×n tunnels (n = 3, 4, 5), which is supported by the XRD pattern for Tod-MnO$_2$ and corresponds well to past reports, but as can be seen in Fig. 4f and Fig. S3b, 3×3 (orange circles) and 3×4 (yellow circles) tunnels dominate the structure. The XRD pattern of Tod-MnO$_2$ (Fig. 3) shows distinct peaks at ~ 9.2° (001) and ~ 18.4° (002) 2θ, corresponding to d-spacings of ~ 9.6 Å and ~ 4.8 Å, respectively. These two peaks are also characteristic of the layered precursor Mg-buserite, which has an interlayer spacing of ~9.6 Å. The XRD pattern for the Mg-buserite precursor is shown in Fig. S4. The cross-sectional STEM images in Fig. 4f reveal that all of the structural tunnels in Tod-MnO$_2$ contain at least one dimension of 3 octahedra (~ 9.6 Å d-spacing), thus resulting in the strong reflections in the XRD pattern corresponding to this tunnel dimension. Moreover, the lack of XRD peaks at lower angles (< 8° 2θ) indicates that there is no systematic presence of tunnels with a side length larger than 3 octahedra, which is supported by their random distribution in the cross-sectional STEM images. Hence, through XRD and cross-sectional STEM, it can be concluded that the structure of the Tod-MnO$_2$ nanowires is composed of tunnels with 3×n dimensions, with the majority of the tunnels consisting of 3×3 and 3×4 octahedra.

Fig. 4g shows a cross-sectional STEM image for the 2×n-MnO$_2$

phase that was synthesized using the HC-Bir precursor with the goal of obtaining the Na-2×3 manganese oxide containing purely 2×3 tunnels. It was found, however, that instead of only 2×3 tunnels being present, 2×2 tunnels (green circles), 2×3 tunnels (red circles), and 2×4 tunnels (blue circles) were each present within a single nanostructure. Additional STEM images (Fig. S3c) show that this configuration of tunnels with the three different dimensions (2×2, 2×3, and 2×4) is systematically present throughout multiple nanowires. As a result of this combination of well-defined tunnel structures that contain a common 2 octahedra dimension, this material is referred to as "2×n-MnO$_2$".

The XRD pattern of 2×n-MnO$_2$ is shown in Fig. 3 along with the literature XRD patterns of Na-2×3 (JCPDS file #14-627) and Na-2×4 [33], as well as experimentally obtained XRD pattern of α-MnO$_2$ (2×2 tunnels). The (001) peak at 9.2° 2θ (~ 9.6 Å, or 3 octahedra tunnel side [33]) for Na-2×3 and (002) peak at 7.4° 2θ (~ 11.9 Å, or 4 octahedra tunnel side [38]) for Na-2×4 are absent in the XRD pattern of the 2×n-MnO$_2$, indicating that there is no ordered presence of these tunnel structures. This conclusion is in agreement with cross-sectional STEM images in Fig. 4g and Fig. S3c that show a random distribution of the 2×3 and 2×4 tunnels. Despite the difference in XRD patterns at lower angles, the XRD pattern of 2×n-MnO$_2$ is constructed by many peaks that overlap with those in the XRD patterns of Na-2×3, Na-2×4, and α-MnO$_2$ phases. A peak at ~12.7° 2θ (~ 7.0 Å), which is indicative of a spacing of 2 octahedra [33], is present in XRD patterns of all four materials. This peak is prominent in the XRD pattern of 2×n-MnO$_2$ due to the systematic and long-range presence of the 2 octahedra tunnel dimension that is seen in the cross-sectional STEM images. Moreover, a multiple of this peak is also found in all four patterns at ~ 25° 2θ.

In addition, there are other common peaks in the XRD patterns of $2 \times n\text{-MnO}_2$, $\alpha\text{-MnO}_2$, Na-2×3, and Na-2×4 phases that correspond to planes of atoms that extend diagonally across and into the tunnel faces ([100] and [010] directions for $\alpha\text{-MnO}_2$ [17], [100] and [001] directions for Na-2×3 and Na-2×4 [33]). All four patterns contain reflections at $\sim 37.5°$, $42.0°$, and $65.5°$ 2θ that correspond to such atomic planes. Further, the $2 \times n\text{-MnO}_2$ shares a common reflection at $\sim 60.0°$ 2θ with $\alpha\text{-MnO}_2$, Na-2×3, and Na-2×4. A summary of these common reflections is shown in Fig. S5. The different miller indices for each material at the same 2θ values are due to the different orientation and size of the unit cells relative to the structural tunnels (see Fig. S1 for crystal structure schematics illustrating unit cell size and orientation). Regardless of the different indices, the presence of these common reflections supports the fact that the structure of the $2 \times n\text{-MnO}_2$ nanowires is indeed similar to that of $\alpha\text{-MnO}_2$, Na-2×3, and Na-2×4. Thus, combined XRD and STEM analysis corroborate that the $2 \times n\text{-MnO}_2$ nanowires have an ordered tunnel structure composed of randomly distributed 2×2, 2×3, and 2×4 tunnels oriented parallel to the longitudinal axis of the nanowire.

Fig. 4h shows the cross-sectional STEM analysis of the Hybrid-MnO_2 nanowires and reveals the tunnel structure of this material to be composed of a highly aperiodic and disordered combination of a number of different tunnel configurations. There are 2×2 tunnels (green circles), 2×3 tunnels (red circles), 3×3 tunnels (orange circles), and even larger structural tunnels including 2×5 (purple circles) all present within a single nanostructure. Additional STEM images (Fig. S3d) show that this type of structure is typical for the entirety of the nanowires, with very little periodicity. There are many areas that are poorly ordered, as well as areas that include tunnels that are not completely formed (yellow box in Fig. 4h). Moreover, the Hybrid-MnO_2 nanowires have a greater degree of surface amorphization compared to the other phases in this work, observed on the edges of the nanowires in the STEM images. As a result of the random and disordered nature of the structural tunnels in this material, it is referred to as "Hybrid-MnO_2". It can also be concluded here that increasing the aging time and thus crystallinity of the Na-birnessite precursor improves the regularity of the structural tunnels within the nanowires. XRD patterns of the LC-Bir and HC-Bir precursors are shown in Fig. S4.

The Hybrid-MnO_2 material is distinct from the $2 \times n\text{-MnO}_2$ due to the greater variety of tunnel configurations, as well as its significantly lower degree of structural order. The XRD pattern of the Hybrid-MnO_2 (Fig. 3) agrees with the STEM images, with fewer, broader peaks present compared to the pattern for the $2 \times n\text{-MnO}_2$. There are also small, broad peaks present at $\sim 6.1°$ 2θ (~ 14.5 Å) and $\sim 8.1°$ 2θ (~ 10.9 Å). Although these peaks do not directly correspond to d-spacings ascribed to 3 and 4 octahedra tunnel side lengths, it is believed that the larger spacing may exist due to a large number of 2×5 tunnels present within the structure, and both peaks indicate a small degree of ordering of larger tunnel dimensions. The Hybrid-MnO_2 XRD pattern is compared to $\alpha\text{-MnO}_2$, Na-2×3, and Na-2×4 in Fig. 3, revealing overlapping peaks between the structures. A peak present at $\sim 12.7°$ 2θ (~ 7.0 Å) is indicative of a spacing of 2 octahedra and in agreement with the cross-sectional STEM images that show a large number of tunnels with a 2 octahedra dimension. There are also peaks in the Hybrid-MnO_2 XRD pattern at $37.5°$ and $65.5°$ 2θ, which were previously shown to be present in the XRD patterns of the $2 \times n\text{-MnO}_2$, $\alpha\text{-MnO}_2$, Na-2×3, and Na-2×4 phases. These peaks indicate that although the Hybrid-MnO_2 contains significantly less order in terms of tunnel dimensions, the structural tunnels seen in the cross-sectional STEM analysis do extend along significant lengths in the nanowires. The order along the longitudinal axis is also supported by the ability to obtain cross-sectional images showing atomic columns of Mn atoms, which would not be possible if the Mn atoms in the walls of the tunnels were disordered along the longitudinal axis of the nanowires. Thus, combined XRD and STEM analysis show that the Hybrid-MnO_2 is a disordered, random combination of structural tunnels with dimensions beyond 2×2, 2×3,

and 2×4.

SEM images of $\alpha\text{-MnO}_2$, Tod-MnO_2, $2 \times n\text{-MnO}_2$, and Hybrid-MnO_2 are shown in Fig. 4a-d. Each material possesses a high aspect ratio, flexible nanowire morphology. The $\alpha\text{-MnO}_2$, Tod-MnO_2, and $2 \times n$-MnO_2 phases consist of nanowires of similar dimensions, with lengths of up to several microns and diameters ranging from 20 to 100 nm. The Hybrid-MnO_2 phase is composed of nanowires with similar lengths as the other three phases but smaller diameters of 10–50 nm, and the smaller diameter indicates the Hybrid-MnO_2 nanowires have a higher surface area than the other three TuMO nanowire phases. The nanowire morphology is believed to be advantageous for water treatment applications since it allows for excellent access of water and ions to material's surfaces. Additionally, nanowires can accommodate larger amounts of strain associated with ion intercalation, an advantage that is characteristic of such nanoscale dimensions [39,40]. The long, flexible nature of the nanowire morphology allows for facile free-standing film formation, which is attractive for the future utilization of these materials in flow-through capacitive deionization devices.

EDX spectra (Fig. S6) reveal the nature and amount of stabilizing ion present within the structural tunnels of the four manganese oxide phases. $\alpha\text{-MnO}_2$ is stabilized by K^+ ions, Tod-MnO_2 is stabilized by Mg^{2+} ions, and both $2 \times n\text{-MnO}_2$ and Hybrid-MnO_2 are stabilized by Na^+ ions. Notably, these stabilizing ions are the same cations as in the salt solutions tested during ion removal (solutions of NaCl, KCl, and MgCl_2). It has been shown that these stabilizing ions not only act as templates for the formation of specific tunnel structures, but also stabilize the structure and facilitate the diffusion of ions during repeated insertion/extraction of the electrochemically cycled ions in energy storage systems [33,41]. As a result, the presence of stabilizing ions in tunnel space is advantageous for repeated ion removal and release. The compositions of the TuMO phases determined via EDX spectra are reported in Table S1. Since the amount of stabilizing ions is relatively small (maximum of 0.25 cation per Mn), there are unoccupied sites within the tunnel structures that provide volume for insertion of ions from solution during HCDI experiments.

3.2. Ion removal capacity

Each of the TuMO phases investigated in this study was tested in 15 mM NaCl, KCl, and MgCl_2 solutions to evaluate the relationship between structural tunnel parameters (size, shape, and distribution of structural tunnels) and ion removal performance. The ion removal capacities (Fig. 5a) were calculated from the concentration vs. time plots shown in Fig. S7. These plots show four complete ion removal/ion release cycles, demonstrating that the four TuMO phases can effectively remove ions from solutions, indicated by a decrease in concentration when a + 1.2 V potential is applied. The cations are removed via electrochemical reaction with the manganese oxide electrode, and the Cl⁻ anions are removed via adsorption onto the activated carbon electrode, similar to the previously reported HCDI systems [9,14]. Moreover, the shape of the concentration vs. time curves corresponds well to previous CDI experiments done in batch mode [8,42]. Upon reversal of the applied potential to − 1.2 V, ions are released back into solution (increase in concentration in Fig. S7), effectively regenerating the electrodes for subsequent ion removal. This regeneration is proven by the following ion removal cycle showing similar behavior to the previous cycle.

Fig. 5a shows the maximum ion removal capacities exhibited by each material in NaCl, KCl, and MgCl_2 solutions. In order to compare capacity values for solutions with different molar masses, the ion removal capacities are normalized by the molar mass of the salt (NaCl, KCl, or MgCl_2), resulting in units of μmol g⁻¹. The same plot shown in Fig. 5a is illustrated in Fig. S8a in mg g⁻¹. Ion removal capacities in both μmol g⁻¹ and mg g⁻¹ are summarized in Table 1. The ion removal capacities exhibited in a given solution varied for each material, indicating that the distinct crystal structure of each material contributes
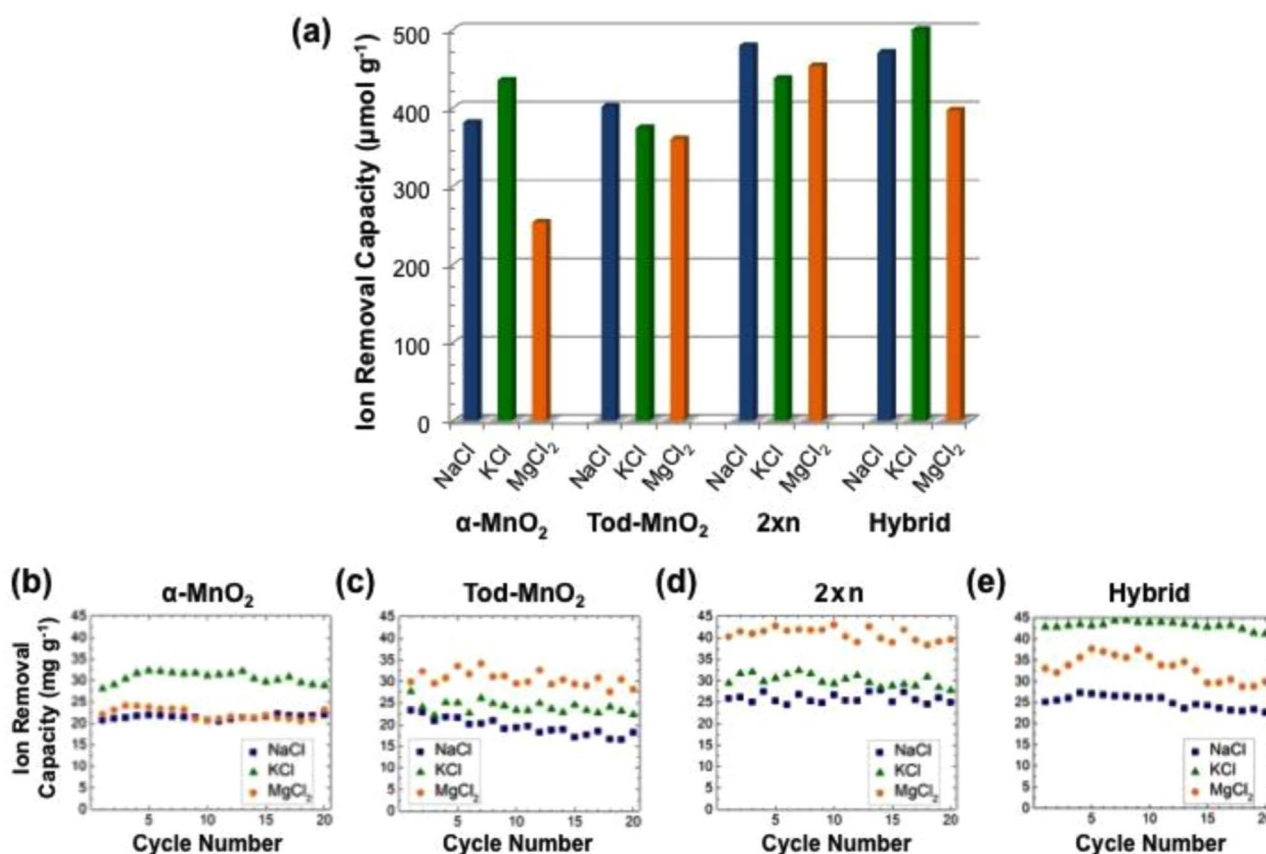
Fig. 5. (a) Maximum ion removal capacities (in µmol g^{-1}) for α-MnO$_2$, Tod-MnO$_2$, 2×n-MnO$_2$, and Hybrid-MnO$_2$ nanowires. (b–e) Ion removal capacities (in mg g^{-1}) through 20 cycles for (a) α-MnO$_2$, (b) Tod-MnO$_2$, (c) 2×n-MnO$_2$, and (d) Hybrid-MnO$_2$.

to the ion removal capacities.

The α-MnO$_2$ nanowires exhibited the highest capacity of 435 µmol g^{-1} (32.2 mg g^{-1}) in a KCl solution and demonstrated lower ion removal capacities in the other two solutions in the order of KCl > NaCl > MgCl$_2$. The Tod-MnO$_2$ nanowires demonstrated the highest capacity of 402 µmol g^{-1} (23.3 mg g^{-1}) in a NaCl solution, with the order of ion removal capacities of NaCl > KCl > MgCl$_2$. The 2×n-MnO$_2$ nanowires achieved the highest capacity of 479 µmol g^{-1} (27.8 mg g^{-1}) in a NaCl solution, with the order of ion removal capacities of NaCl > MgCl$_2$ > KCl, while the Hybrid-MnO$_2$ nanowires achieved the highest capacity of 600 µmol g^{-1} (44.4 mg g^{-1}) in KCl solution, with the order of ion removal capacities of KCl > NaCl > MgCl$_2$. The α-MnO$_2$ and Hybrid-MnO$_2$ nanowires demonstrated their highest respective capacities in KCl solution, while the Tod-MnO$_2$ and 2×n-MnO$_2$ nanowires demonstrated their highest respective capacities in NaCl solution.

The two TuMO phases with the most variety in terms of tunnel dimensions, the 2×n-MnO$_2$ and Hybrid-MnO$_2$ nanowires, showed the highest overall ion removal capacities. The highest capacity of 479 µmol g^{-1} (27.8 mg g^{-1}) in a NaCl solution and the highest capacity of 454 µmol g^{-1} (43.1 mg g^{-1}) in a MgCl$_2$ solution was exhibited by the 2×n-MnO$_2$ phase, and the highest capacity of 600 µmol g^{-1} (44.4 mg g^{-1}) in a KCl solution was exhibited by the Hybrid-MnO$_2$ phase. The two materials contain larger structural tunnels than the α-MnO$_2$ nanowires, and it can be seen that both the 2×n-MnO$_2$ and Hybrid-MnO$_2$ nanowires achieve higher capacities than the α-MnO$_2$ nanowires in each solution. These results suggest that larger structural tunnels allow for improved ion removal capacities compared to smaller structural tunnels. Thus, efficient deionization of brackish water may require a crystalline material with a distribution of tunnel sizes for not only maximum ion removal capacity in a given solution, but also for effective removal of ionic species with varying radii from solution.

Following the trend of larger ion removal capacities for materials with larger structural tunnels, it would be expected that the Tod-MnO$_2$ nanowires would demonstrate the highest ion removal capacities in each solution tested due to the larger 3×3 and 3×4 tunnels. However, our results show that the ion removal capacities exhibited by the Tod-MnO$_2$ are lower than that of the 2×n-MnO$_2$ and Hybrid-MnO$_2$ phases (Table 1). This phenomena was attributed to the divalent nature of the

Table 1

Maximum ion removal capacities in µmol g^{-1} (and mg g^{-1}) and maximum ion removal rates in µmol g^{-1} s^{-1} (and mg g^{-1} s^{-1}) for α-MnO$_2$, Tod-MnO$_2$, 2×n-MnO$_2$, and Hybrid-MnO$_2$ nanowires in an HCDI cell in 15 mM solutions of NaCl, KCl, and MgCl$_2$.

Material	α-MnO$_2$			Tod-MnO$_2$			2×n-MnO$_2$			Hybrid-MnO$_2$		
Salt solution	*NaCl*	*KCl*	*MgCl$_2$*	*NaCl*	*KCl*	*MgCl$_2$*	*NaCl*	*KCl*	*MgCl$_2$*	*NaCl*	*KCl*	*MgCl$_2$*
Maximum ion removal capacity (µmol g^{-1}) (mg g^{-1})	**381**	**435**	**254**	**402**	**374**	**360**	**479**	**438**	**454**	**471**	**600**	**397**
	22.1	*32.2*	*24.1*	*23.3*	*27.7*	*34.2*	*27.8*	*32.4*	*43.1*	*27.3*	*44.4*	*37.7*
Maximum ion removal rate (µmol g^{-1} s^{-1}) (mg g^{-1} s^{-1})	**1.91**	**1.82**	**1.73**	**1.93**	**1.78**	**1.69**	**1.60**	**1.61**	**1.72**	**0.80**	**2.23**	**1.24**
	0.111	*0.135*	*0.164*	*0.112*	*0.132*	*0.161*	*0.093*	*0.119*	*0.163*	*0.046*	*0.165*	*0.118*

stabilizing Mg^{2+} ions in the Tod-MnO_2 structure, as opposed to monovalent stabilizing ions (Na^+ and K^+ ions) in the other three TuMO phases. Assuming that the electrochemical activity of TuMO phases during ion removal is associated with the Mn^{4+} to Mn^{3+} reduction induced by insertion of positively charged ions from the salt solution, higher ion removal capacities can be expected for the manganese oxide phase with the higher manganese oxidation state. Stabilizing ions in the TuMO nanowires, however, partially reduce the manganese oxidation state. The oxidation state of manganese in the four TuMO phases in this work was evaluated from the chemical composition analysis (Table S1). The lower oxidation state of manganese calculated for Tod-MnO_2 is likely to reduce its ion removal capacity, despite the large structural tunnels, which is in agreement with our experimental results. Therefore, the nature of the stabilizing ions plays an important role in the HCDI performance of TuMO phases.

To further evaluate the relationship between structural tunnel size and ion removal capacity in each solution, ion removal capacities for all TuMO phases were compared to both the ionic and hydrated radii of the three cations in solution (radii shown in the legend in Fig. 1). It was found that the ion removal capacities of the TuMO nanowires correlated with the hydrated radii of the ions being removed from solution, rather than the ionic radii. The lowest capacity for α-MnO_2 nanowires in $MgCl_2$ solution indicates that the smaller 2×2 tunnels do not favor the removal of the cations with the largest hydrated radius, Mg^{2+} ions. The Tod-MnO_2, which contains larger 3×3 and 3×4 structural tunnels, notably demonstrates higher capacities in $MgCl_2$ solutions, indicating that the larger tunnel structures allow for improved removal of larger hydrated cations. This trend is supported well by the capacities of the $2 \times n$-MnO_2, which in addition to containing the 2×2 tunnels characteristic of α-MnO_2 nanowires, also contains 2×3 and 2×4 tunnels. The $2 \times n$-MnO_2 nanowires demonstrate nearly the same capacity as α-MnO_2 in a KCl solution, but in NaCl and $MgCl_2$ solutions, the nanowires achieve higher ion removal capacities than α-MnO_2 nanowires (26% increase in NaCl solution and 79% increase in $MgCl_2$ solution, Table 1). Moreover, the Hybrid-MnO_2 nanowires also exhibit higher ion removal capacities in NaCl and $MgCl_2$ solutions compared to the α-MnO_2 nanowires (Table 1). Thus, these results show that the smaller tunnels do not favor the removal of larger hydrated cations, while the larger tunnels allow for enhanced removal of larger hydrated cations compared to the smaller tunnels.

The ion removal capacities of the four manganese oxides over 20 ion removal/ion release cycles are shown in Fig. 5b–e. Concentration vs. time plots (Fig. S7) show that the HCDI electrodes can repeatedly remove ions from solution and subsequently regenerate by releasing ions back into solution, with stable capacities exhibited through 20 cycles for all materials in NaCl, KCl, and $MgCl_2$ solutions. The slight variability in capacity is attributed to the dynamic nature of the flowing system and has been observed in the past for deionization systems with ion-exchange membranes [43]. The structural stability of the TuMO phases was verified by XRD analysis of the electrodes after 20 ion removal/ion release cycles (Fig. S9). Comparison of the XRD patterns of the pristine and cycled electrodes revealed that the crystal structure of each material is maintained after 20 ion removal/ion release cycles in NaCl, KCl, and $MgCl_2$ solutions, indicating promising structural stability of TuMO phases in electrochemical systems in aqueous media. The cycling plots shown in Fig. 5b–e demonstrate the feasibility of using redox active TuMO nanowires as HCDI electrodes, since the electrodes can repeatedly remove and release ions from solution, maintaining high ion removal capacities.

The charge efficiencies of the TuMO nanowires in HCDI experiments are shown in Fig. S10. The charge efficiency is a ratio of the amount of salt removed from solution to the amount of charge passed through the electrode [5,6], where a higher charge efficiency corresponds to lower energy consumption [6]. The amount of salt removed is calculated by converting the ion removal capacity to moles of salt removed, and the amount of charge passed through the electrode is calculated by

integrating the current signal with respect to time during ion removal cycles (current vs. time plots shown in Fig. S11). It can be seen in the plots of charge efficiency vs. cycle number (Fig. S10) that for all materials tested, the charge efficiency of the device remains above 80% in each solution. For the α-MnO_2 nanowires, lower charge efficiency is observed in $MgCl_2$ solution. Notably, this is the same solution in which this material exhibited its lowest ion removal capacities, further supporting the observation that the smaller tunnels are not efficient for the removal of larger ions from the solution. Also, the material with the highest overall ion removal capacity in both NaCl and $MgCl_2$ solutions, $2 \times n$-MnO_2, demonstrated the most stable values of charge efficiency. On the other hand, the Tod-MnO_2 nanowires showed more sporadic behavior in terms of charge efficiency, and the Hyrbid-MnO_2 nanowires also showed less stable behavior after 10 cycles in NaCl and $MgCl_2$ solutions. However, in a KCl solution (in which the Hybrid-MnO_2 nanowires exhibited the highest overall ion removal capacity), the charge efficiency of the Hybrid-MnO_2 remains stable at above 90% over 20 cycles. Although factors such as the cell geometry, operational parameters, and the inclusion of both the anion and cation exchange membranes can improve charge efficiency in a given (H)CDI cell [43,44], the high values obtained in this work further demonstrate the efficacy of using TuMO nanowires as electrodes in HCDI.

The desalination mechanism of TuMO nanowires was investigated via analysis of electrode chemical composition before and after ion removal experiments. EDX spectra, used to evaluate M:Mn (M = Na, K, Mg) ratio, are shown in Fig. S12 for the pristine electrodes and for electrodes that were stopped at the end of the ion removal step after 20 ion removal/ion release cycles. The EDX spectra clearly show the presence of peaks for Na, K, and Mg after electrodes were tested in NaCl, KCl, and $MgCl_2$ solutions, respectively, suggesting that the cations removed from solution are chemically bound in the crystal structure of the manganese oxides. These results indicate that the mechanism of ion removal is based on a redox process, either intercalation of the cations into the crystal structures of the materials or redox pseudocapacitance. Further explanation of the ion removal mechanism of the TuMO phases can be found in Section 4. The EDX spectra also show that the stabilizing ions (K^+ ions for α-MnO_2, Mg^{2+} ions for Tod-MnO_2, and Na^+ ions for $2 \times n$-MnO_2 and Hybrid-MnO_2) remain in the structure after ion removal experiments and thus are not released into solution.

To investigate the role of the carbon electrode in this system, EDX analysis was performed on the activated carbon electrodes before and after ion removal experiments. Cycled electrodes were analyzed before and after washing with copious amounts of deionized water. The EDX spectra of the cycled activated carbon electrodes (Fig. S13), which were stopped after the ion removal step, show a clear Cl peak. No other peaks related to the cations in solution are present, indicating that the carbon does remove only the Cl^- ions. After washing of the electrode, the Cl peak in the EDX spectrum disappears, confirming that the Cl^- ions are removed from solution via adsorption in the electric double layer on the surface of the activated carbon, which agrees with past reports on the mechanism of ion removal in CDI [5,6]. Hence, the two electrodes in the HCDI system remove ions from solution via two different mechanisms, with the manganese oxide electrodes removing ions via redox reactions and the carbon electrodes via formation of the electric double layer.

3.3. Ion removal rate

Further investigation into the process of ion removal was made by calculating the ion removal rates for each material/solution combination in this study. This parameter is calculated from the instantaneous ion removal capacity (in $\mu mol\ g^{-1}$ or $mg\ g^{-1}$) divided by the step time (s) and represents the speed at which ions are removed from solution [9]. The maximum ion removal rates in $\mu mol\ g^{-1}\ s^{-1}$ (normalized for molar mass of the salts being removed) are shown in Fig. 6a. The same values are shown in Fig. S8b with the units of $mg\ g^{-1}\ s^{-1}$ for

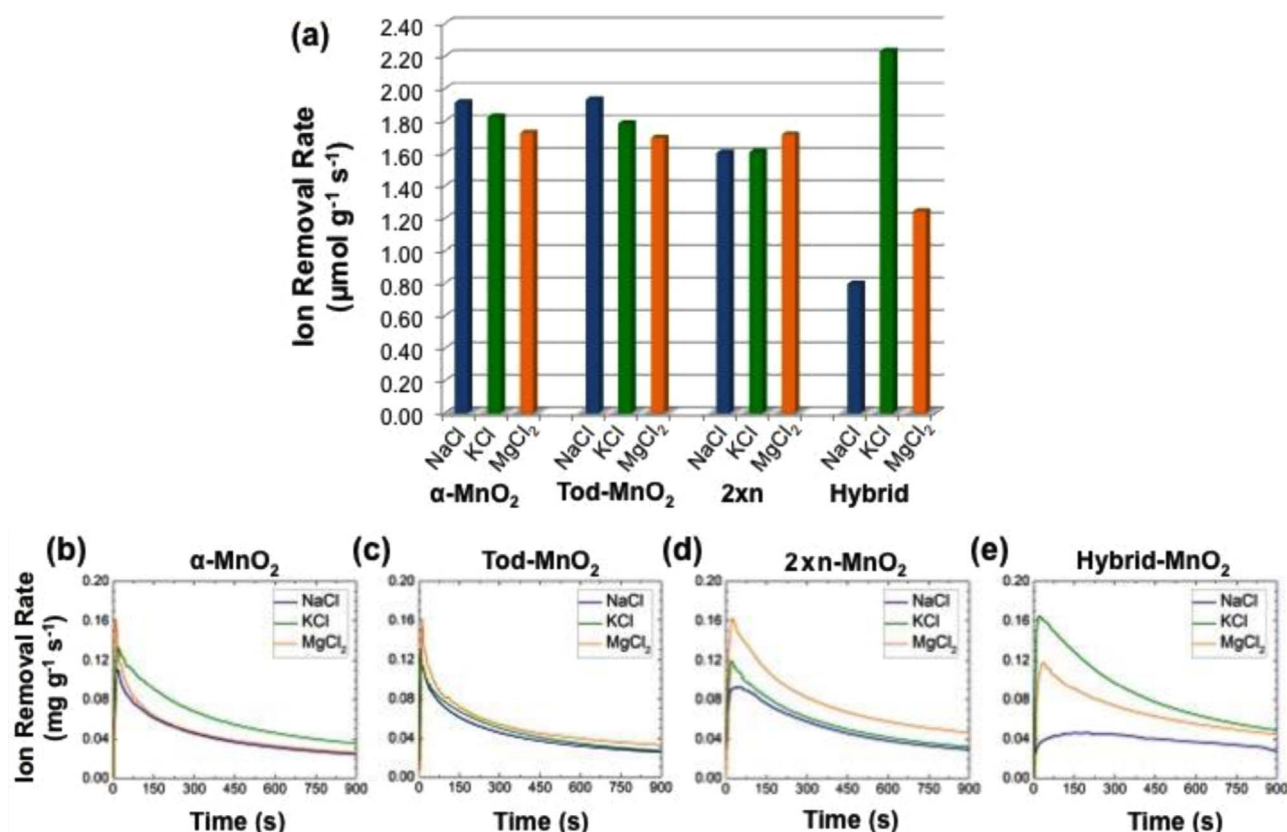**Fig. 6.** (a) Ion removal rates for α-MnO$_2$, Tod-MnO$_2$, 2×n-MnO$_2$, and Hybrid-MnO$_2$ nanowires expressed in µmol g^{-1} s^{-1}. (b–e) Ion removal rate (in mg g^{-1} s^{-1}) vs. time plot for one ion removal cycle for (a) α-MnO$_2$, (b) Tod-MnO$_2$, (c) 2×n-MnO$_2$, and (d) Hybrid-MnO$_2$.

comparison and summarized in Table 1 (in both µmol g^{-1} s^{-1} and mg g^{-1} s^{-1}). We found that the three materials with more well-defined crystal structures, α-MnO$_2$, Tod-MnO$_2$, and 2×n-MnO$_2$, exhibited comparable ion removal rate behavior across all solutions tested. Each material achieved similar ion removal capacities in the range of 1.69–1.93 µmol g^{-1} s^{-1} in solutions of NaCl, KCl, and MgCl$_2$.

Plots of ion removal rate vs. cycle time for one ion removal cycle (Fig. 6b–e, in mg g^{-1} s^{-1}) show that the α-MnO$_2$ and Tod-MnO$_2$ nanowires exhibit similar ion removal behavior, with the ion removal rate quickly increasing within the first 30 s and then steadily decreasing and approaching a lower limit throughout the rest of the 15 min cycle. This behavior corresponds to the fast initial removal of cations and anions by the manganese oxide and carbon electrodes, respectively, followed by slowing ion removal through the remainder of the cycle as the electrodes become saturated. Combined with the fact that α-MnO$_2$, Tod-MnO$_2$, and 2×n-MnO$_2$ nanowires demonstrate similar ion removal capacities, these results indicate a similar mechanism of ion removal for materials with more well-defined structures. Moreover, the ion removal rate vs. time curve in Fig. 6b for α-MnO$_2$ in a KCl solution is different from the curves for α-MnO$_2$ in NaCl and MgCl$_2$ solutions in that the ion removal rate value does not decrease as quickly after the maximum value is achieved. Higher ion removal rates are maintained for a longer period of time in KCl solution, and this correlates with α-MnO$_2$ exhibiting its highest capacity in KCl solution. Likewise, for the other three TuMO phases, higher ion removal capacities correlate with higher ion removal rates maintained for longer periods of time.

The Hybrid-MnO$_2$ nanowires exhibited slightly different ion removal patterns compared to the other TuMO phases in this work. Notably, the Hybrid-MnO$_2$ nanowires demonstrated a much higher ion removal rate of 2.23 µmol g^{-1} s^{-1} in a KCl solution (Fig. 6e), and a higher ion removal rate is maintained throughout the whole cycle. These results are in good agreement with the highest overall ion

removal capacity of 600 µmol g^{-1} exhibited by Hybrid-MnO$_2$ nanowires in a KCl solution. In NaCl and MgCl$_2$ solutions, though, the Hybrid-MnO$_2$ nanowires demonstrated lower ion removal rates of 0.80 µmol g^{-1} s^{-1} and 1.24 µmol g^{-1} s^{-1}, respectively. However, as was the case in a KCl solution, higher ion removal rates were maintained throughout the whole cycle, resulting in comparatively high ion removal capacities for this material. This observation is particularly apparent in a NaCl solution, where the lowest overall ion removal rate is achieved, but this rate is maintained without the sharp decrease that is observed for all other material/solution combinations. These results indicate different ion removal behavior for the Hybrid-MnO$_2$ nanowires that consists of continuous removal of Na$^+$ ions from solution at a constant rate throughout the whole cycle. This difference is also evident in the slope of the concentration vs. time plot for the Hybrid-MnO$_2$ nanowires in NaCl solution (Fig. S7).

We believe that the different ion removal rate behavior observed for the Hybrid-MnO$_2$ nanowires (both the markedly higher ion removal rate in KCl solution and the constant ion removal rate in NaCl solution throughout the cycle) is a result of several materials parameters that distinguish the Hybrid-MnO$_2$ nanowires from the three TuMO phases with more well-defined crystal structures. As described in Section 3.1, the Hybrid-MnO$_2$ nanowires exhibit smaller diameters, a greater degree of surface amorphization, and a much more disordered and distorted structure that could result in tortuous and discontinuous diffusion pathways. The combination of larger, more open tunnels and tortuous ion diffusion pathways may result in the slower ion removal rates but relatively high ion removal capacities observed for the Hybrid-MnO$_2$ nanowires in both NaCl and MgCl$_2$ solutions. However, this does not explain the high ion removal rate observed in KCl solution, for which there seems a beneficial relationship between the K$^+$ ion and the structure and morphology of the Hybrid-MnO$_2$ nanowires that results in superior ion removal behavior. More work is needed to fully understand

Table 2

Ion removal capacities and ion removal rates of (a) carbon and carbon/metal oxide composite electrodes in NaCl solution, (b) faradaic electrodes used in an HCDI configuration in NaCl solution, and (c) carbon electrodes in KCl and MgCl$_2$ solutions reported in the literature. Capacities and ion removal rates of TuMO phases in this work are shown in (b) and (c) for reference.

(a) Carbon and carbon/metal oxide composite electrodes in NaCl solution

Material	Cell configuration	Voltage (cycle length)	Exchange membranes	Solution strength (mM)	Flow rate (mL min⁻¹)	Capacity (mg g⁻¹)	Ion Removal Rate	Ref
Activated carbon	CDI	1.2 V (30 min)	None	2	NR	10.4	NR	[49]
Activated carbon	MCDI	1.2 V (15 min)	Anion and cation	10	10	22.4	0.072 mg g⁻¹ s⁻¹	[9]
Nitrogen-doped graphene sponge	CDI	1.2 V (40 min)	None	8.6	27	21.0	NR	[8]
Activated carbon/TiO$_2$	CDI	1.2 V (30 min)	None	5	22	17.4	NR	[45]
Graphene aerogel/TiO$_2$	CDI	1.2 V (7 min)	None	8.6	30	15.1	NR	[50]
Graphene/MnO$_2$ nanorods	CDI	1.2 V (120 min)	None	1.3	NR	5.01	NR	[51]
MWCNTs/MnO$_2$	Opposite carbon	1.8 V (25 min)	None	1.2	15	6.65	NR	[52]
Nanoporous carbon/MnO$_2$	CDI	1.2 V (50 min)	None	0.9	20	0.98	NR	[53]

(b) Faradaic electrodes in NaCl solution

Material	Cell configuration	Voltage (cycle length)	Exchange membranes	Solution strength (mM)	Flow rate (mL min⁻¹)	Capacity (mg g⁻¹)	Ion removal rate	Ref
Na$_{0.44}$MnO$_2$	Opposite carbon (HCDI)	1.2 V (15 min)	Anion	10	10	31.2	0.066 mg g⁻¹ s⁻¹	[9]
Na$_2$FeP$_2$O$_7$	Opposite carbon (HCDI)	1.2 V (15 min)	Anion	10	2	30.2	0.081 mg g⁻¹ s⁻¹	[14]
FeFe(CN)$_6$	Opposite carbon (HCDI)	Constant current @20 C to 1.4 V (5.5 min)	Anion and cation	~ 17	650	40.8	0.2925 mg g⁻¹ s⁻¹	[46]
MWCNT·hV$_2$O$_5$	Opposite carbon (HCDI)	0.8 V (60 min)	Anion and cation	200	5	~ 26	NR	[54]
Exfoliated MoS$_2$	Opposite carbon (HCDI)	1.2 V (75 min)	None	50	NR	4.41	NR	[47]
α-MnO$_2$	Opposite carbon (HCDI)	1.2 V (15 min)	Anion and cation	15	20	22.1	0.111 mg g⁻¹ s⁻¹	This Work
Tod-MnO$_2$	Opposite carbon (HCDI)	1.2 V (15 min)	Anion and cation	15	20	23.3	0.112 mg g⁻¹ s⁻¹	This Work
2×n-MnO$_2$	Opposite carbon (HCDI)	1.2 V (15 min)	Anion and cation	15	20	27.8	0.093 mg g⁻¹ s⁻¹	This Work
Hybrid-MnO$_2$	Opposite carbon (HCDI)	1.2 V (15 min)	Anion and cation	15	20	27.3	0.046 mg g⁻¹ s⁻¹	This Work

(c) Carbon electrodes in KCl and MgCl$_2$ solutions

Material	Cell configuration	Voltage (cycle length)	Exchange membranes	Solution strength (mM)	Flow rate (mL min⁻¹)	Capacity KCl (µmol g⁻¹)	Capacity MgCl$_2$ (µmol g⁻¹)	Ref
Activated carbon	CDI	1.0 V (until saturated)	None	16	10	195	117	[55]
Activated carbon	CDI	1.2 V (30 min)	None	2	NR	197	–	[49]
α-MnO$_2$	Opposite carbon (HCDI)	1.2 V (15 min)	Anion and cation	15	20	435	254	This Work
Tod-MnO$_2$	Opposite carbon (HCDI)	1.2 V (15 min)	Anion and cation	15	20	374	360	This Work
2×n-MnO$_2$	Opposite carbon (HCDI)	1.2 V (15 min)	Anion and cation	15	20	438	454	This Work
Hybrid-MnO$_2$	Opposite carbon (HCDI)	1.2 V (15 min)	Anion and cation	15	20	600	397	This Work

the complex structure of the Hybrid-MnO$_2$ phase and how it relates to the effective removal of ions from KCl solution.

4. Discussion

The performance of TuMO nanowires in this work compare favorably with those reported for both CDI and HCDI systems in the past. Table 2a shows the ion removal capacities and ion removal rates of carbon and carbon/metal oxide composites reported in earlier works. Ion removal capacities as high as 21.0 mg g^{-1} and 17.4 mg g^{-1} have been demonstrated by nitrogen-doped graphene sponge and composite activated carbon/TiO$_2$ electrodes, respectively [8,45], in NaCl solutions with similar concentrations to this work. In an MCDI system, values as high as 22.4 mg g^{-1} have been reported with carbon electrodes [9].

In Table 2b, the ion removal capacities and ion removal rates of the TuMO phases presented here are compared to several other reports on faradaic electrode materials utilized in an HCDI configuration with activated carbon as the opposite electrode. Past reports on HCDI systems demonstrated capacities of up to 31.2 mg g^{-1} for the metal oxide Na$_{0.44}$MnO$_2$ and 40.8 mg g^{-1} for the Prussian blue compound FeFe(CN)$_6$ in NaCl solutions [9,46]. In this work, capacities of 22.1, 23.3, 27.8, and 27.3 mg g^{-1} were achieved for α-MnO$_2$, Tod-MnO$_2$, 2×n-MnO$_2$, and Hybrid-MnO$_2$ nanowires in NaCl solution, respectively. Although parameters such as the cell configuration, applied potential, ion exchange membranes, solution strength, and flow rate vary between reports, it can be seen that the ion removal capacity of the TuMO nanowires studied in this work is consistent with the other faradic materials investigated thus far for electrochemical water desalination. While in Table 2b only comparison of static electrode HCDI systems is made, an HCDI cell architecture based on manganese oxide deposited on carbon opposite a carbon flow electrode demonstrated promising performance in overcoming the saturation limit of the carbon [48]. Such flow-electrode architecture represents the ability to investigate the capacity of manganese oxides without the limit of the carbon counter, and TuMOs can potentially exhibit even higher ion removal capacities in such a system compared to the performance reported here.

Regarding ion removal rate and ion removal capacity in beyond NaCl solutions (KCl and MgCl$_2$), TuMO nanowires demonstrate superior performance to previously reported materials (Table 2c). For the first time, we show the behavior of the HCDI system in beyond NaCl solutions. The scarce studies on the behavior of carbon electrodes in solutions beyond NaCl reported ion removal capacities of 190 μmol g^{-1} and 197 μmol g^{-1} for activated carbon in KCl solutions in CDI systems and a capacity of 117 μmol g^{-1} for activated carbon in a MgCl$_2$ solution [49,55]. The TuMO nanowires in this work exhibit capacities two to three times larger than the values for activated carbon in KCl and MgCl$_2$ solutions. This high performance is particularly important for desalination of brackish water that contains a number of ionic species beyond NaCl.

An advantage of HCDI is its fast deionization rates that are comparable to carbon based systems, and the magnitude of the maximum deionization rates achieved in this work is higher than those reported for Na$_{0.44}$MnO$_2$ and Na$_2$FeP$_2$O$_7$ in NaCl solutions (0.074 mg g^{-1} s^{-1} and 0.081 mg g^{-1} s^{-1}, respectively) [9,14]. Markedly higher values were achieved in NaCl for α-MnO$_2$, Tod-MnO$_2$, and 2×n-MnO$_2$ nanowires (Table 2b), and this can be partially attributed to the incorporation of the cation exchange membrane, which can facilitate improved ion removal rates [34] and agrees well with the high ion removal rates demonstrated by the Prussian blue compound FeFe(CN)$_6$ in a system containing both anion and cation exchange membranes [46]. Nonetheless, such high ion removal rates were also achieved for the TuMO nanowires in KCl and MgCl$_2$ solutions, demonstrating the effectiveness of the materials at quickly removing ions from solution in the HDCI configuration.

The fast ion removal rates demonstrated by the TuMO nanowires in this work indicate that an additional mechanism beyond the diffusion-limited intercalation of ions into the crystal structures of the TuMO phases contributes to the ion removal capacity. The charge storage mechanism of manganese oxides has been extensively investigated in the past [18,26,56–58], and in aqueous solutions, it has been shown that manganese oxides can react with cations in a solution through two distinct mechanisms. The first mechanism is the adsorption of cations onto the surface of the manganese oxides, resulting in pseudocapacitive behavior, and the second mechanism is the intercalation of cations into the crystal structure of the materials, with both mechanisms involving a change of the oxidation state of Mn. For the TuMO phases in this work, despite the similar morphologies and thus available surfaces of the α-MnO$_2$, Tod-MnO$_2$, and 2×n-MnO$_2$ nanowires, different ion removal capacities were obtained for each material/solution combination. The differing capacities indicate that the ion removal capacity is not dependent strictly on the surfaces of the TuMO nanowires, and the crystal structures of these materials likely contribute to the ion removal process as well, with ions from solution intercalating into the structural tunnels of the manganese oxides. This is supported by past reports proving that ions from aqueous solution intercalate into the crystal structures of TuMO phases [59,60], as well as by past reports on birnessite MnO$_2$ that have shown both surface pseudocapacitance and intercalation reactions can occur in manganese oxides [56,59,61,62]. Moreover, TuMO nanowires have been shown in the past to have relatively modest surface areas ($\sim$ 30 to 65 m^2 g^{-1}) [38,63–65], and therefore, the large ion removal capacities achieved from these materials cannot be purely surface based, considering that materials with significantly higher surfaces areas (i.e. porous carbons) achieve lower ion removal capacities [5,6,66].

We believe that both pseudocapacitance and intercalation contribute to the ion removal capacities of the TuMO nanowires studied in this work. The high ion removal rates achieved by the TuMO phases, and how quickly such rates occur after the application of a positive potential, indicate that the pseudocapacitive mechanism may dominate ion removal at first. This fast ion removal step is likely to be followed by a diffusion-limited intercalation of ions into the structural tunnels of the TuMO nanowires. This intercalation process leads to the high ion removal capacities obtained in these materials and defines differences between the capacities of the different structures. This proposed mechanism of ion removal makes manganese oxides very attractive for HCDI because of their combined high ion removal rate and high capacities. However, more detailed study of the proposed mechanism is necessary to fully understand the process by which ions are removed from solution.

With each material demonstrating distinct capacities in the three solutions tested in this work, it presents the idea of tailoring the crystal structures of faradaic materials to specific ion removal applications. There is a need for materials with crystal structures that can selectively remove targeted ions from natural or wastewater sources, as well as a need for materials that can effectively remove a range of ionic species from solution. Tailoring structures to these specific applications will require the development of a better understanding of the relationship between the ion removal mechanism of the active materials (i.e. diffusion-limited intercalation or pseudocapacitance), the free volume available within a crystal structure for ion removal, and the relative size of the ionic species to be removed. In terms of tunnel manganese oxides, by understanding the relationship between tunnel size, shape, and ionic content, the performance of these materials can be optimized for either maximum ion removal capacity or selective ion removal. The results shown here demonstrate that smaller structural tunnels do not favor the removal of larger hydrated cations such as Mg^{2+}. Moreover, the larger tunnels allow for greater removal of larger hydrated cations compared to smaller tunnels. Thus, it is expected that as the ion size increases, such as for inorganic and organic pollutants, the relationship between structural tunnel size and ion size will be critical for maximum ion removal capacities. This logic can also be extended to materials with other tailorable crystal structures, such as layered materials in which

interlayer spacing can be carefully controlled. By manipulating inter-layer spacing, it may be possible to achieve not only high ion removal capacities, but also a large degree of selectivity. Hence, through careful crystal structure engineering and understanding of the ion removal mechanisms, the performance of redox active electrodes for HCDI can be further enhanced.

5. Conclusion

In this work, for the first time, we demonstrate the use of redox active TuMO nanowires as efficient electrodes for hybrid capacitive deionization. The performance of four TuMO phases, including two never previously reported before materials with ordered and disordered combinations of structural tunnels with different dimensions, was investigated in NaCl, KCl, and MgCl$_2$ solutions. High ion removal capacities were achieved for all material/solution combinations, demonstrating the effectiveness of the manganese oxides for brackish water desalination. It was shown that in the HCDI system, the manganese oxide electrodes remove ions via chemical reaction with the host crystal structure while the carbon electrodes store ions from solution on the surface in the electric double layer. Moreover, high ion removal rates (up to 0.011 mg g^{-1} s^{-1} in NaCl solution) were achieved due to the fast redox processes occurring in the TuMO nanowires. Our results demonstrate that in aqueous electrochemical systems the crystal structures of the active materials should be tailored to the hydrated radius of the ions in solution, not ionic radius. It was found that the moderate ability of the α-MnO$_2$ nanowires, which contain smaller structural tunnels, to remove larger hydrated Mg^{2+} ions can be overcome by increasing the tunnel size, as demonstrated by the performance of Tod-MnO$_2$, 2 × n-MnO$_2$, and Hybrid-MnO$_2$ phases with larger tunnels. Thus, TuMO nanowires were shown to be a promising family of materials for application as faradaic electrode materials for water desalination via HCDI.

Acknowledgements

Appendix A. Supplementary material

Supplementary data associated with this article can be found in the online version at http://dx.doi.org/10.1016/j.nanoen.2017.12.015.

References

[1] M.M. Mekonnen, A.Y. Hoekstra, Sci. Adv. 2 (2016).
[2] In Inisght Report, World Economic Forum, Geneva, Switzerland, 2017.
[3] P.H. Gleick, Water in Crisis: A Guide to the World's Fresh Water Resources, Oxford University Press, Inc., New York, New York, 10016, 1993.
[4] M.A. Anderson, A.L. Cudero, J. Palma, Electrochim. Acta 55 (2010) 3845–3856.
[5] S. Porada, R. Zhao, A. van der Wal, V. Presser, P.M. Biesheuvel, Prog. Mater. Sci. 58 (2013) 1388–1442.
[6] M.E. Suss, S. Porada, X. Sun, P.M. Biesheuvel, J. Yoon, V. Presser, Energy Environ. Sci. 8 (2015) 2296–2319.
[7] Q. Jiang, Y. Han, W. Tang, H. Zhu, C. Gao, S. Chen, M. Willander, X. Cao, Z. Lin Wang, Nano Energy 15 (2015) 266–274.

[8] X. Xu, Z. Sun, D.H.C. Chua, L. Pan, Sci. Rep. 5 (2015) 11225.
[9] J. Lee, S. Kim, C. Kim, J. Yoon, Energy Environ. Sci. 7 (2014) 3683–3689.
[10] F. La Mantia, M. Pasta, H.D. Deshazer, B.E. Logan, Y. Cui, Nano Lett. 11 (2011) 1810–1813.
[11] J. Lee, S.H. Yu, C. Kim, Y.E. Sung, J. Yoon, Phys. Chem. Chem. Phys. 15 (2013) 7690–7695.
[12] M. Pasta, A. Battistel, F. La Mantia, Energy Environ. Sci. 5 (2012) 9487–9491.
[13] M. Pasta, C.D. Wessells, Y. Cui, F. La Mantia, Nano Lett. 12 (2012) 839–843.
[14] S. Kim, J. Lee, C. Kim, J. Yoon, Electrochim. Acta 203 (2016) 265–271.
[15] J.E. Post, Proc. Natl. Acad. Sci. USA 96 (1999) 3447–3454.
[16] Y. Chabre, J. Pannetier, Prog. Solid State Chem. 23 (1995) 1–130.
[17] M.M. Thackeray, Prog. Solid State Chem. 25 (1997) 1–71.
[18] S. Devaraj, N. Munichandraiah, J. Phys. Chem. C 112 (2008) 4406–4417.
[19] J. Yuan, W.N. Li, S. Gomez, S.L. Suib, J. Am. Chem. Soc. 127 (2005) 14184–14185.
[20] Y.T. Wang, A.H. Lu, H.L. Zhang, W.C. Li, J. Phys. Chem. C 115 (2011) 5413–5421.
[21] Q. Feng, H. Kanoh, Y. Miyai, K. Ooi, Chem. Mater. 7 (1995) 1722–1727.
[22] Z.H. Liu, K. Ooi, Chem. Mater. 15 (2003) 3696–3703.
[23] B.W. Byles, P. West, D.A. Cullen, K.L. More, E. Pomerantseva, RSC Adv. (2015) 106265–106271.
[24] M.J. Duncan, F. Leroux, J.M. Corbett, L.F. Nazar, J. Electrochem. Soc. 145 (1998) 3746–3757.
[25] J. Huang, A.S. Poyraz, S.Y. Lee, L. Wu, Y. Zhu, A.C. Marschilok, K.J. Takeuchi, E.S. Takeuchi, ACS Appl. Mater. Interfaces 9 (2017) 4333–4342.
[26] D. Bélanger, L. Brousse, J.W. Long, Electrochem. Soc. Interface 17 (2008) 49–52.
[27] H.U. Sverdrup, M.W. Johnson, R.H. Fleming, The Oceans: Their Physics, Chemistry, and General Biology 7 Prentice-Hall, New York, 1942.
[28] P. Xu, J.E. Drewes, D. Heil, G. Wang, Water Res. 42 (2008) 2605–2617.
[29] R. Shannon, Acta Crystallogr. Sect. A: Cryst. Phys. Diffr. Theor. Gen. Crystallogr. 32 (1976) 751–767.
[30] E.R. Nightingale, J. Phys. Chem. 63 (1959) 1381–1387.
[31] Y. Gao, Z. Wang, J. Wan, G. Zou, Y. Qian, J. Cryst. Growth 279 (2005) 415–419.
[32] Z.H. Liu, L. Kang, K. Ooi, Y. Makita, Q. Feng, J. Colloid Interface Sci. 285 (2005) 239–246.
[33] X.F. Shen, Y.S. Ding, J. Liu, J. Cai, K. Laubernds, R.P. Zerger, A. Vasiliev, M. Aindow, S.L. Suib, Adv. Mater. 17 (2005) 805–809.
[34] P.M. Biesheuvel, R. Zhao, S. Porada, A. van der Wal, J. Colloid Interface Sci. 360 (2011) 239–248.
[35] S. Bodeï, A. Manceau, N. Geoffroy, A. Baronnet, M. Buatier, Geochim. Cosmochim. Acta 71 (2007) 5698–5716.
[36] X.H. Feng, W.F. Tan, F. Liu, J.B. Wang, H.D. Ruan, Chem. Mater. 16 (2004) 4330–4336.
[37] Z. Sun, H. Chen, D. Shu, C. He, S. Tang, J. Zhang, J. Power Sources 203 (2012) 233–242.
[38] G.G. Xia, W. Tong, E.N. Tolentino, N.G. Duan, S.L. Brock, J.Y. Wang, S.L. Suib, T. Ressler, Chem. Mater. 13 (2001) 1585–1592.
[39] L. Mai, X. Tian, X. Xu, L. Chang, L. Xu, Chem. Rev. 114 (2014) 11828–11862.
[40] X. Ma, W. Luo, M. Yan, L. He, L. Mai, Nano Energy 24 (2016) 165–188.
[41] Y. Yuan, C. Zhan, K. He, H. Chen, W. Yao, S. Sharifi-Asl, B. Song, Z. Yang, A. Nie, X. Luo, H. Wang, S.M. Wood, K. Amine, M.S. Islam, J. Lu, R. Shahbazian-Yassar, Nat. Commun. 7 (2016) 13374.
[42] Y. Liu, X. Xu, M. Wang, T. Lu, Z. Sun, L. Pan, Chem. Commun. 51 (2015) 12020–12023.
[43] A. Omosebi, X. Gao, J. Landon, K. Liu, ACS Appl. Mater. Interfaces 6 (2014) 12640–12649.
[44] R. Zhao, P.M. Biesheuvel, A. van der Wal, Energy Environ. Sci. 5 (2012) 9520–9527.
[45] P. Srimuk, M. Zeiger, N. Jäckel, A. Tolosa, B. Krüner, S. Fleischmann, I. Grobelsek, M. Aslan, B. Shvartsev, M.E. Suss, V. Presser, Electrochim. Acta 224 (2017) 314–328.
[46] L. Guo, R. Mo, W. Shi, Y. Huang, Z.Y. Leong, M. Ding, F. Chen, H.Y. Yang, Nanoscale 9 (2017) 13305–13312.
[47] F. Xing, T. Li, J. Li, H. Zhu, N. Wang, X. Cao, Nano Energy 31 (2017) 590–595.
[48] S. Hand, R.D. Cusick, Environ. Sci. Technol. 51 (2017) 12027–12034.
[49] Y. Li, C. Zhang, Y. Jiang, T.J. Wang, H. Wang, Desalination 399 (2016) 171–177.
[50] H. Yin, S. Zhao, J. Wan, H. Tang, L. Chang, L. He, H. Zhao, Y. Gao, Z. Tang, Adv. Mater. 25 (2013) 6270–6276.
[51] A.G. El-Deen, N.A.M. Barakat, H.Y. Kim, Desalination 344 (2014) 289–298.
[52] B. Chen, Y. Wang, Z. Chang, X. Wang, M. Li, X. Liu, L. Zhang, Y. Wu, RSC Adv. 6 (2016) 6730–6736.
[53] J. Yang, L. Zou, H. Song, Z. Hao, Desalination 276 (2011) 199–206.
[54] J. Lee, P. Srimuk, K. Aristizabal, C. Kim, S. Choudhury, Y.-C. Nah, F. Mücklich, V. Presser, ChemSusChem (2017).
[55] C.H. Hou, C.Y. Huang, Desalination 314 (2013) 124–129.
[56] T. Brousse, D. Bélanger, J.W. Long, J. Electrochem. Soc. 162 (2015) A5185–A5189.
[57] J.K. Chang, M.-T. Lee, W.T. Tsai, J. Power Sources 166 (2007) 590–594.
[58] M. Toupin, T. Brousse, D. Bélanger, Chem. Mater. 16 (2004) 3184–3190.
[59] O. Ghodbane, F. Ataherian, N.L. Wu, F. Favier, J. Power Sources 206 (2012) 454–462.
[60] O. Ghodbane, J.L. Pascal, F. Favier, ACS Appl. Mater. Interfaces 1 (2009) 1130–1139.
[61] L. Athouël, F. Moser, R. Dugas, O. Crosnier, D. Bélanger, T. Brousse, J. Phys. Chem. C 112 (2008) 7270–7277.
[62] L. Yang, S. Cheng, J. Wang, X. Ji, Y. Jiang, M. Yao, P. Wu, M. Wang, J. Zhou, M. Liu, Nano Energy 30 (2016) 293–302.
[63] P. Nithyadharseni, M.V. Reddy, H. Fanny, S. Adams, B.V.R. Chowdari, RSC Adv. 5 (2015) 60552–60561.
[64] X. Shen, Y. Ding, J. Liu, K. Laubernds, R.P. Zerger, M. Polverejan, Y.C. Son,

M. Aindow, S.L. Suib, Chem. Mater. 16 (2004) 5327–5335.

[65] A.S. Poyraz, J. Huang, S. Cheng, D.C. Bock, L. Wu, Y. Zhu, A.C. Marschilok, K.J. Takeuchi, E.S. Takeuchi, Green Chem. 18 (2016) 3414–3421.

[66] Y. Liu, C. Nie, X. Liu, X. Xu, Z. Sun, L. Pan, RSC Adv. 5 (2015) 15205–15225.

Bryan W. Byles received his bachelor's degree in Materials Science and Engineering from Rutgers University in 2013. Bryan is currently a 4th year Ph.D. candidate at Drexel University in the Department of Materials Science and Engineering, advised by Dr. Ekaterina Pomerantseva. His research focuses on investigating the performance of tunnel structured manganese oxides for electrochemical energy and water treatment applications.

Dr. David A. Cullen is the R&D Staff Scientist and Team Leader in the Electron Microscopy Group of the Materials Science and Technology Division at Oak Ridge National Laboratory. He is also a joint faculty member in the Bredesen Center for Interdisciplinary Research and Graduate Education at the University of Tennessee, Knoxville. He received a B.S. degree in Applied Physics from Brigham Young University, and a Ph.D. in Materials Science and Engineering from Arizona State University. He joined ORNL in 2010 as an Alvin M. Weinberg Fellow. His current research interests are focused on the advanced characterization of fuel cell catalysts by electron microscopy, but also include a wide range of collaborations through the Center for Nanophase Materials Sciences user program.

Dr. Karren L. More is the Group Leader for the Electron and Atom Probe Microscopy Group in the Center for Nanophase Materials Sciences (CNMS) at Oak Ridge National Laboratory (ORNL). She received her Ph.D. from North Carolina State University and has been a research staff member at ORNL since 1988, first in the Materials Science and Technology Division, and more recently (since 2013) at the CNMS. Her research interests are focused on using advanced electron microscopy towards understanding the structure and chemistry of nanomaterials, especially related performance, stability, and durability.

Dr. Ekaterina Pomerantseva is Anne Stevens Assistant Professor of Materials Science and Engineering at Drexel University. She received a B.S. degree in Materials Science in 2000 and M.S. degree in Chemistry and Materials Science in 2003 from Lomonosov Moscow State University, a M.S. degree in Biochemistry in 2005 from McGill University, and a Ph.D. degree in Solid-State Chemistry in 2007 from Lomonosov Moscow State University. She held postdoctoral appointments at the University of Maryland College Park (2010–2013) and the University of Waterloo (2009–2010). She has co-authored over 45 journal papers. Her research interests lie in the development and characterization of novel nanostructured materials for batteries, pseudocapacitors and water treatment with the goal to better understand intercalation-based electrochemical processes at nanoscale.